UAB
Universitat Autònoma de Barcelona

Dipòsit digital de documents de la UAB

This is the **submitted version** of the journal article:

Kubovics, Márta [et al.]. «Green Supercritical CO2 Synthesis of [Copper Clusters@FeBTC]@rGO Catalyst for Highly Efficient Hydrogenation of CO2 to Methanol». *ACS sustainable chemistry & engineering*, Vol. 12, Num. 28 (July 2024), p. 10634-10646 DOI 10.1021/acssuschemeng.4c03656

This version is available at https://ddd.uab.cat/record/329270

under the terms of the IN COPYRIGHT license.

Green supercritical CO_2 synthesis of [copper clusters@FeBTC]@rGO catalyst for highly efficient hydrogenation of CO_2 to methanol

Márta Kubovics,[1*] Alejandro Borrás,[1] Ahmad Abo Markeb,[2,3] Gregorio Marbán,[4] Javier Moral-Vico,[2] Antoni Sánchez,[2] Ana M. López-Periago,[1] Concepción Domingo,[1*]

[1] Materials Science Institute of Barcelona (ICMAB-CSIC), Campus UAB, 08193 Bellaterra (Spain) E-mail: mkubovics@icmab.es, conchi@icmab.es

[2] Department of Biological Chemistry and Environmental Engineering (UAB), Campus UAB, 08193 Bellaterra (Spain)

[3] Carbon Science and Technology Institute (INCAR-CSIC), C/Francisco Pintado Fe 26, 33011 Oviedo (Spain)

Abstract

In the vast majority of studies, methanol production *via* CO_2 hydrogenation is realized using bifunctional catalysts, commonly CuZnO phases. The basic motivation of this study is to confront main concerns regarding typical copper-based catalysts, which are the aggregation of the active metal nanoparticles and its concomitant deactivation. For this, an extensive research on composites of mesoporous iron trimesate MOFs (crystalline MIL-100(Fe) and semiamorphous FeBTC), loaded with copper clusters (CuCs) into the pores, is here performed, being this study pioneer in the area. The growth and aggregation of CuCs are hindered by the confinement of the active entities into the MOF mesocages. From the two studied MOFs, only the copper loaded semiamorphous FeBTC behaves as a catalyst. To further enhance the catalytic activity, CuCs@FeBTC NPs are dispersed on the plates constituting a reduced graphene-oxide (rGO) aerogel. Main steps in the preparation of these complex catalysts involve the use of sustainable technology based on supercritical CO_2, used either as a solvent or drying agent. The reduction strategy designed to obtain the active catalyst (Cu^{2+} to Cu^{+}/Cu^{0} in CuCs)

was crucial to upgrade the end product performance. A double reduction route, applying ascorbic acid preceding thermal H_2 reduction, turns out to be necessary to attain a significant catalytic activity of the confined Cu^{2+} species. The as-synthetized and spent catalysts were analyzed in regard of the structure (X-ray diffraction, infrared), bulk (mass spectrometry) and surface (X-ray photoelectron spectroscopy) composition, morphology (microscopy and energy dispersive spectroscopy) and textural properties (N_2 physisorption). The catalytic performance of reduced CuCs@FeBTC and [CuCs@FeBTC]@rGO composites was tested in the CO_2 hydrogenation reaction at 10 bar. Methane and methanol were obtained as valuable reaction products. When using the [CuCs@FeBTC]@rGO aerogel, methanol yield was noticeably high, in comparison to reported data, in the order of 86 $mg_{MeOH}g_{Cu}^{-1}h^{-1}$; while the amount of side products (methane, CO) was almost totally hindered up to 260 °C.

1. Introduction

Massive demand for goods and energy, together with population's lack of recognition of current climate emergency, are disturbing the ecological equilibrium of Earth. In the last decades, CO_2 concentration in the atmosphere, linked to climate change, has increased continuously due to the growing energy demand that is mainly supplied by fossil fuels and carbon.[1] It is widely recognized that mitigation of emitted CO_2 is essential to decelerate greenhouse effect. Ahead from CO_2 capture, there are two essential pathways expressed to contribute to the reduction of CO_2 present in the atmosphere. Formerly, the most evident tactic involves moving towards green industrial technologies.[2] For this reason, the concept of sustainable manufacturing[3] is becoming increasingly important, with a focus on reducing the vast quantities of consumed organic solvents.[4] Since the use of solvents is frequently unavoidable, reduced solvent impact comes by replacing concern by green solvents, the latter represented essentially by water, ionic liquids or supercritical CO_2 ($scCO_2$) and few carefully chosen traditional organic solvents.[5-7] The second approach consists in re-utilizing CO_2 through its direct conversion into added-value chemicals.[8] A large variety of different products, from hydrocarbons to oxygenated carbons, such as methane (CH_4), short-chain olefins, aromatics, methanol (MeOH) or ethanol (EtOH), are chemically produced using CO_2 as a reagent. In these processes, CO_2 is not considered waste product, but a C1 chemical feedstock. This research addresses the two factors stated for CO_2 mitigation, *e.g.*, the use of CO_2 as a solvent for synthesis and the re-use of CO_2 for goods production. In point of fact, the main objective of this investigation is the $scCO_2$ green synthesis of catalytic materials optimized for the hydrogenation of CO_2 to MeOH and/or CH_4, both molecules scrutinized as renewable fuels. MeOH is of particular interest for the production of biofuels due to its high energy density, with additional advantages related to easy storing.[9] Methanation processes using waste CO_2 and renewably-sourced H_2 offers an alternative to natural gas extraction with low carbon footprint.[10]

CO_2 reduction with H_2 implies the use of a catalyst that must be selected properly to design a sustainable catalytic design.[11] Currently, catalysis is known to play a major role at mitigating the environmental impact of chemical industry by radically reducing energy and materials consumption. Typically, the CO_2 hydrogenation reaction comprises a catalyst with active metal sites dispersed on a support, all together offering an immense variety of possibilities.[12] Overall, Cu/ZnO-based catalysts are used for MeOH production, while composites containing transition (Fe, Co, Ni) or noble (Pd, Ru, Rh) metals have been investigated in methanation reactions.[13] The use of inexpensive, earth-abundant, non-noble metals as catalysts should be favored, not only by economic reasons, but also because of the significantly minor negative impact on the environment.[14] The use of a support is necessary to increase the dispersion of the metal active centers in the bulk catalyst, as well as to improve the electronic properties of the metal, providing further advantages by increasing the selectivity and the conversion. Porous oxides (alumina, silica or zirconia), carbides, zeolites, carbon-based compounds (activated carbon, graphene, carbon nanotubes, *etc*) and polymers are frequently used supports.[15-18]

Recently, metal-organic frameworks (MOFs) have been introduced in the area of catalysis as a new class of materials that can simultaneously have functions of both, active center and support.[19] MOFs are porous materials constituted by metallic nodes and polytopic organic linkers, which can be designed with high structural and thermal stability, large internal pore volume and an interconnected network of pores. Some examples of reactions involving CO/CO_2 performed using MOF catalysts are alkene hydrogenation, epoxidation or oligomerization, the synthesis of N-heterocycles mediated by transition metals-based catalysts,[20,21] as well as those involving water (dehydration or esterification).[22] The archetypical microporous UiO-66, HKUST-1 and ZIF-8 -with Zr_6O_8, Cu_2 and Zn nodes, respectively- and the mesoporous NU-1000, MOF-5 and MIL-100 family -with Zr_6O_8, Zn_4O and $Al_3O/Fe_3O/Cr_3O$ nodes, respectively- have prominently been investigated in the area of

MOF catalysis, either as pristine compounds (Fig. 1a) or by forming composites with active metal particles (Fig. 1b).[23,24] In some cases, net MOFs (Fe, Cu, *etc*) can straightforwardly be used as catalysts thanks to the inherent internal network of metal nodes, *e.g.*, by involving various oxidation states (Fig. 1aI).[25] To increase the catalytic capabilities, or to make a MOF catalytically active, these compounds can be subjected to a post-synthetic reaction usually to modify the linker by addition of basic/acid groups, functional molecules or active centers to missing-linkers defects (Fig. 1aII).[26-28] MOFs with mixed metal nodes acting as catalyst can be straightforwardly obtained by synthesis or by post-transmetalation (Fig. 1aIII).[29,30] The catalytic activity in MOFs can be attained by composing them with species that are not part of the framework, but are dispersed in the bulk, e.g., by adding metallic nanoparticles (NPs) that can be either covering the surface of the MOF particles (Fig. 1bI) or forming core-shell structures in which the MOF grows surrounding the catalyst (Fig. 1bII).[31,32]

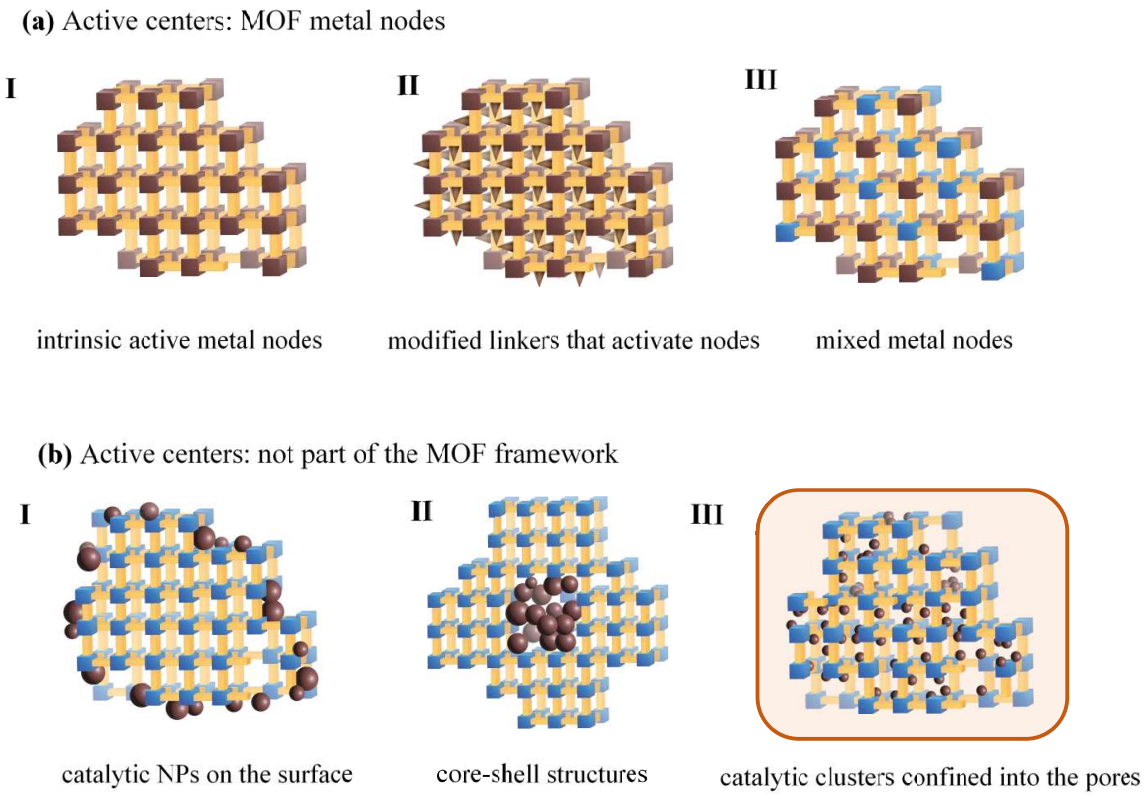

Figure 1. Schematic representation of diverse structures of MOFs used in catalysis: (a) net MOFs, and (b) composite MOFs with active catalyst NPs or clusters.

Recently, two new vectors have emerged in the MOFs arena for catalyst design. On one side, the so-called ultradispersed catalysts have been described, involving the confinement of catalytically active metal units/clusters (*e.g.* Cu/Zn, Pd or Pt) into the MOF pores (Fig. 1bIII).[33-35] Only MOFs with large pore size, *e.g.*, mesoporous MOFs, are susceptible of being impregnated with metal clusters, and still to remain accessible for the diffusion of the reagents and products of the catalytic reaction. On the other side, the relevance of semiamorphous MOFs is currently recognized based on the presence of intrinsic structural defects, *e.g.*, metal vacancies or missed linkers, often leading to improved catalytic activity.[36] Based on the described premises, this work aims to achieve significant progress in the fundamental understanding of a new category of composites involving semiamorphous mesoporous MOFs loaded with catalytically active units into the pores. Iron trimesate mesoporous MOFs (crystalline MIL-100 and semiamorphous FeBTC) are chosen for analysis because of their noticeable capacity for CO_2 adsorption, thus facilitating catalytic reactions involving this gas, *e.g.*, the reaction of CO_2 hydrogenation. Particularly, FeBTC impregnated with copper clusters (CuCs) is taken as the case study. The particulate CuCs@FeBTC catalyst can be further dispersed in a meso/macroporous support to improve the catalytic activity. Aerogels of reduced graphene oxide (rGO) are chosen for this purpose, based in the previously demonstrated efficacy of this support.[17] The advantages of the $scCO_2$ technology in regard of processing porous compounds are used here in several of the preparation steps necessary to obtain the [CuCs@FeBTC]@rGO product, *e.g.*, to synthesize FeBTC, to infuse the metal catalyst precursor into the pore channels of the MOF and to shape the GO aerogel composite. The reduction stage of the metal precursor (Cu^{2+}) to the active catalyst (Cu^{+}/Cu^{0}) turned out to be the key to design a proper material for an effective catalytic reaction. Gas phase (H_2) and liquid phase (ascorbic acid) reduction routes were tested. ~~Extensive~~ Solid-state characterization of the pristine and spent catalysts was performed to understand the catalytic behavior. This work is

motivated by the design of a CO_2 hydrogenation process economically attractive and energetically sustainable carried out at low pressure (*e.g.*, 10-15 bar).[17,18] In this respect, this study provides useful guidance in determining catalysts and operating conditions for the reaction. Results evidenced that the design of a two-step reduction route was crucial to maximize the efficiency of the composite, while the addition of GO had ~~an enormous~~ relevance in methanol selectivity. Particularly, the best results were obtained with the catalyst involving copper clusters impregnated in FeBTC and using as a support rGO, with MeOH production rates in the order of 86 $mg_{MeOH}g_{Cu}^{-1}h^{-1}$ and MeOH selectivity's nearly 100 wt% at 260 ºC and 10 bar, which is the highest value of MeOH production found to data in experiments performed at such a low pressure.[17,18]

2. Materials and methods

2.1. Materials

Iron nitrate monohydrate ($Fe(NO)_3.9H_2O$), trimesic acid (H_3BTC), copper acetylacetonate ($Cu(acac)_2$), and ascorbic acid (aa, $C_6H_8O_6$), were purchased from Sigma Aldrich-Merck , and utilized as reagents for MOF preparation, metal catalyst precursor and reduction agent, respectively. Regarding the used solvents, dioxane was provided by PanReac, while ethanol was delivered by Scharlau. In all cases, the chemicals were used as-received without further characterization, while stored in a chemical cabinet. For synthesis, the reagents were weighed on a laboratory scale (A&D Instruments GR-200-EC) with accuracy 1 mg. For aerogel preparation, a GO dispersion in water (4 $mgmL^{-1}$) was purchased from Graphenea S.A. Pressurized CO_2 (99.95 wt%), used for composite synthesis, H_2 (99.97 wt%), applied for catalyst reduction, and CO_2/H_2 mixture (mole ratio 1:3), consumed during the catalytic experiments, were all delivered by Carburos Metálicos S.A.

2.2. Methods

2.2.1. Synthesis of FeBTC

The preparation of FeBTC was carried out following a reported procedure.[37] Briefly, a gel precursor was prepared in 1.5 mL of dioxane by mixing H_3BTC (0.20 g) and $Fe(NO_3)_3.9H_2O$ (0.58 g) in a molar ratio of 1:1.5, and was further dried in a stirred high-pressure reactor (TharDesign, 100 mL volume), loaded with $scCO_2$ at 200 bar and 70 ºC, recorded with a pressure transducer (± 1 MPa) and a thermocouple (± 1 ºC), respectively, during 48 h. Detailed description of the reactor and procedure can be found in ref. 37. After isothermal depressurization and cooling, a dry orange powder was recovered, which was washed by centrifugation first with water (30 mL) and then twice with EtOH (30 mL) at 10000 rpm during 10 min, and finally dried overnight in a vacuum desiccator. The MOF was activated under high vacuum (*ca.* 0.1 bar) at 150 ºC during 20 h to remove residual traces from the pores, thus obtaining a brown powder. For comparison, the crystalline counterpart of FeBTC, the MIL-100(Fe) phase, was also synthesized. The preparation procedure is detailed in the SI.

2.2.2. Synthesis of $Cu(acac)_2$@FeBTC

A $scCO_2$ method was used to prepare the $Cu(acac)_2$@FeBTC composite. For this, a 100 mL high-pressure reactor was loaded with 200 mg of activated MOF, wrapped with a filter paper (Labbox Prat dumas hardened quantitative filter paper, slow flow rate, pore 7-9 μm, thickness 290 μm) and 200 mg of $Cu(acac)_2$, placed into a glass beaker together with a stir bar. The set-up is schematized in Fig. 2a. The reactor was sealed and filled with $scCO_2$ at 200 bar and 80 ºC, conditions that were maintained under stirring (200 rpm) for 72 h. After depressurizing and cooling the system, the composite sample was recovered from the paper bag.

2.2.3. Synthesis of CuCs@FeBTC

Two different procedures were used for the reduction of $Cu(acac)_2$@FeBTC, with the objective of achieving a significant Cu^{2+} reduction. In the first method (Fig. 2bI), the reduction process

was carried out in a tubular column (0.45×9 cm id×l) holding the powder (*ca.* 150 mg) distributed over glass wool. The sample was subjected during 2 h to a flow of H_2 (20 $mLmin^{-1}$) at 260 °C. Samples were labeled as $[CuCs@FeBTC]_{H2}$. In the second approach (Fig. 2bII), an extra liquid-reduction procedure was performed before H_2 treatment. For this purpose, 125 mg of the precursor were dispersed in 20 mL of EtOH by sonication, to which *ca.* 100 mg of ascorbic acid were added. The reduction reaction was induced by microwave heating (Anton Paar Monowave 400) at 100 ºC for 5 min, while stirring the vial vigorously. The obtained reddish dispersion was washed thrice with ethanol until the supernatant became colorless, and then filtered. The precipitate was dried under vacuum, recovering a powder that was added to the previously described tubular reactor. The $[CuCs@FeBTC]_{aa}$ sample was further reduced with H_2 at 300 °C for 2 h to synthetize the $[CuCs@FeBTC]_{aaH2}$ catalyst.

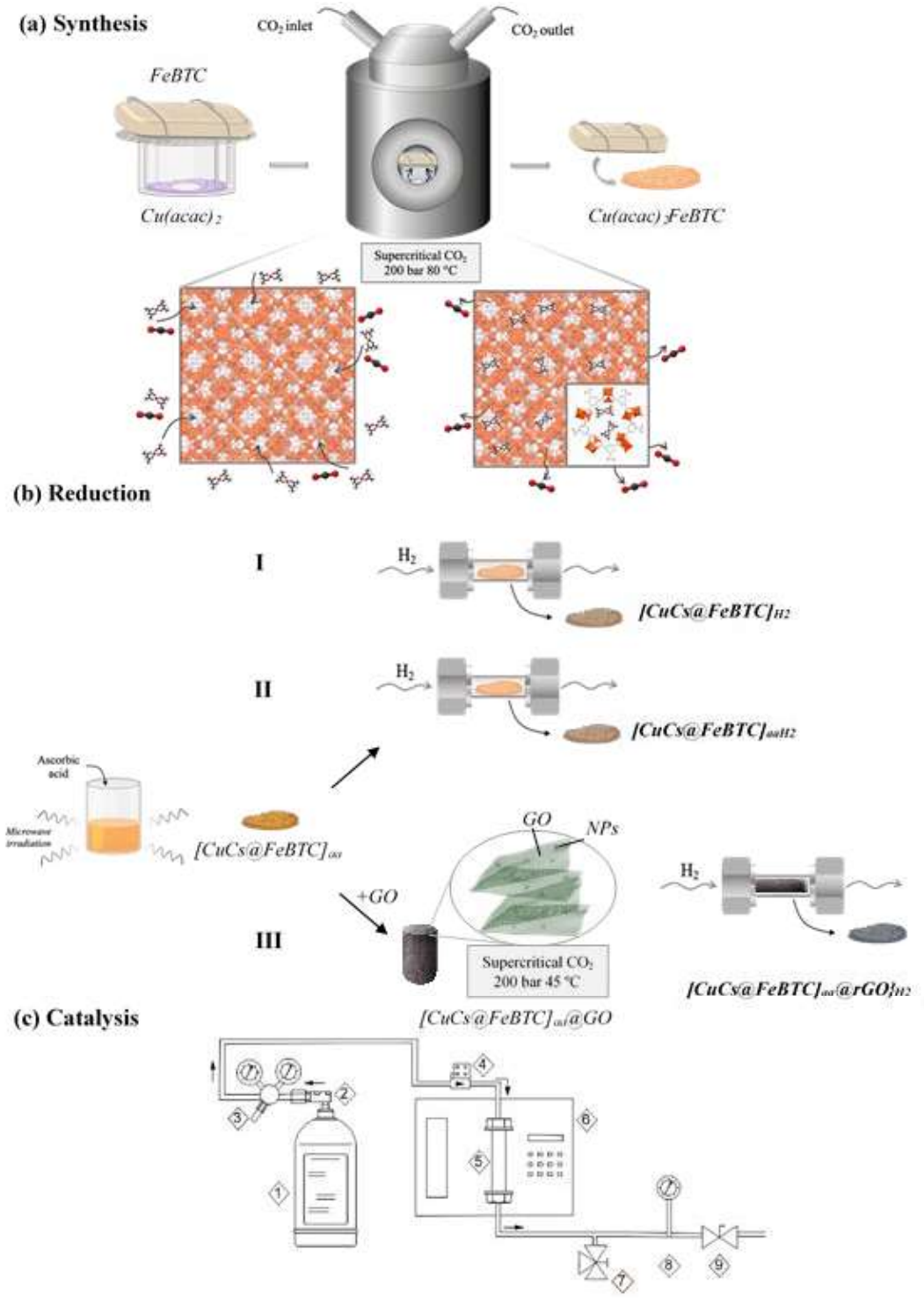

Figure 2. Schematic representation of the used procedures and equipment for: (a) synthesis of the precursor $Cu(acac)_2$@FeBTC, (b) reduction routes, (I) H_2 for $[CuCs@FeBTC]_{H2}$, (II) ascorbic acid and H_2 for $[CuCs@FeBTC]_{aaH2}$, and (III) ascorbic acid and H_2 for $\{[CuCs@FeBTC]_{aa}@rGO\}_{H2}$, and (c) catalysis.

2.2.3. Synthesis of [CuCs@FeBTC]@rGO

The double reduction route was followed in this case (Fig. 2bIII). First, 150 mg of the $[CuCs@FeBTC]_{aa}$ powder were ultrasonically dispersed in 5 mL of GO in EtOH (*ca.* 3.5 $mgmL^{-1}$).[38] Then, the resulting dense dispersion was poured in vials of 1 mL and placed in a high-pressure reactor. To eliminate the EtOH phase, the sample was dried in $scCO_2$ at 200 bar and 45 °C for 48 h. Finally, the system was isothermally depressurized and aerogel monoliths of $[CuCs@FeBTC]_{aa}@GO$ were obtained. The monoliths were broken into small pieces using a spatula, and added to the previously described tubular reactor. The sample was then reduced with H_2 at 260 °C for 2 h, thus preparing the $\{[CuCs@FeBTC]_{aa}@rGO\}_{H2}$ catalyst.

2.3. Structural characterization

The as-synthesized and spent catalysts were characterized using mainly solid-state techniques. The structural characterization was carried out by powder X-ray diffraction (XRD) in a Siemens D5000 diffractometer, using Cu Kα incident radiation with a step scan of 0.01°. Fourier transform infrared-attenuated total reflection (FTIR-ATR) spectroscopy (Jasco 4700 Spectrophotometer) was used to ascertain the molecular composition of the sample surface. The textural properties were determined by N_2 adsorption/desorption isotherms acquired at -196 ºC (ASAP 2020 Micromeritics Inc). The t-method was used to determine the micropore volume (V_{mp}). The surface area (S_a) was determined with the Brunauer-Emmet-Teller (BET) equation, while the Barrett-Joyner-Halenda (BJH) method was applied to estimate the pore volume (V_p) from the adsorption branch of the isotherm. For weight measurements, a Sartorius QUINTIX224-1S analytical balance (accuracy 0.1 mg), placed in a specific balance table, is used. This balance has a fully automatic internal calibration system (isoCAL), although periodic manual checks are carried out with standards of known weight. Before weighing, the balance is washed thoroughly to eliminate any interference in the measurement (debris, dust), finalizing with vacuum cleaning. The correct weighing of the sample (before and after

degassing) is extremely important to give the results of the textural values per unit of mass. Weighing is carried out in the absence of any air stream to avoid generating any type of air turbulence in the weighing cabin, in a room maintained at *ca*. 20 ºC. During measurements, it is checked that the weight of the sample does not vary over time due to electrostatic effects. To partially alleviate these effects, the balance has been lined with aluminum foil, so that almost the entire interior part of the balance, and even the tube support, are at the same electrical potential and the movement of the charged particles is minimized. Further, an antistatic kit universal from Mettler Toledo, which generates an emission of ions in the tip is used to discharge the statically charged sample and the tare tube containers. Under these conditions, each sample is tared and weighed inside the tube an average of 15 times, giving the mean value as the precise weight. Thermogravimetric analysis (TGA, SDT 650 TA instruments) was carried out under N_2 flow (50 $mLmin^{-1}$) up to a temperature of 500 ºC. The morphology of the composites was investigated by scanning electron microscopy (SEM, Quanta FEI 200). For particular samples, elemental atomic mappings were recorded in a scanning/transmission electron microscope (STEM, XHRSEM FEI Magellan 400 L) by using energy dispersive spectroscopy (EDS, X–Max Ultim Extreme EDX Oxford Inst.) with a resolution of *ca.* 1 nm. To further study the elemental distribution, a Gemini II column on a Zeiss crossbeam equipped with an EDS system (Oxford Ultim Max) was used. Copper and iron contents were quantitatively determined in reduced samples by inductively coupled plasma mass spectrometry (ICP-MS, Agilent 7700x), after high temperature solid digestion in a mixture of hydrochloric, nitric and hydrofluoric acids (3:1:0.5 v/v). *Ex-situ* X-ray photoelectron spectroscopy (XPS) of the powdered samples, previously compacted into disc-shaped tablets, was carried out on a Specs spectrometer, using monochromatic Al-Kα radiation emitted from a double anode at 12 kV and 200 W. Measurements were carried out to determine the oxidation

state of the copper in the reduced samples, as well as any potential modification of the iron valence in the MOF (see SI for technical description).

2.4. Catalytic activity tests

Catalytic activity tests were carried out in a hand made equipment settle by Process Integral Development Engineered & Tech. (Fig. 2c). The equipment involves a pressurizer cylinder (1) loaded with H_2:CO_2, which, through an open/close valve (2) and a pressure regulator (3), deliver the gas mixture to the area in which the reaction takes place. The gas flow is regulated and measured by using a mass flow meter (4, Bronkhorst mini Cori-flow). The catalytic activity of the CO_2 hydrogenation was evaluated in a stainless steel fixed bed reactor (5) with an internal diameter of 0.45 and a length of 9 cm. The reactor is connected to the system by two vespel and graphite ferrules and settle inside an oven of a 7890A Agilent gas chromatograph (6). The exhausted flow pass trough a three-way needle valve (7) used to take aliquots at fixed periods of time in a sample bag (SKC FlexFoil PLUS Sample Bag). At the exit, a manometer (8) was used to measure system pressure. A ball valve was used to depressurized the system (9). For the analyzed samples, measurements were straightforwardly performed in the fixed-bed tubular column used for H_2 reduction, just by switching the flow of pure H_2 to a mixture of CO_2/H_2. The pressure was set at 10 bar, while the gas flow rate was fixed at 10 $mLmin^{-1}$. After the steady state was reached (*ca*. 20 min), ejected products were determined by collecting three aliquots at each settle temperature: 180, 200, 220, 240 and 260 ºC. The chosen H_2/CO_2 molar ratio was 3:1. MeOH was measured using a Shimadzu GC-2010 gas chromatograph with a flame ionization detector. Helium was used as carrier gas, and the software used was Chromeleon (Version 6.80 SR5b). The inlet and the detector temperature were 260 °C and 280 °C respectively, and the inlet flow was 50 $mLmin^{-1}$. The production of CO_2, CH_4 and CO was quantified using an Agilent Tech. 7890B gas chromatograph with a thermal conductivity detector and He as a carrier gas. OpenLab (Version A.01.04) was the software used, and the

inlet temperature and flow were 120 °C and 20 mLmin^{-1}, respectively. The detector temperature was at 150 ºC. All the temperatures were measured with a thermocouple with an accuracy of ± 1 ºC. During this reaction, presumably other hydrocarbons with longer chains might also be formed, but in small quantities and were not quantified.[39] MeOH and CH_4 space-time yields (STY) were estimated by copper weight to facilitated comparison with literature data. CO_2 conversion and selectivity between MeOH and CH_4 *vs.* CO were parameters calculated to assess the catalytic performance of the synthesized samples.

3. Results and discussion

3.1. Catalyst precursors synthesis and characterization

Even though this work focuses on using of semiamorphous FeBTC as a metal catalyst support, the synthesis and analysis of crystalline MIL-100(Fe) were also performed for comparison. The description of the synthetic method for the later, as well as the results of the structural (Fig. S1), morphological (Fig. S2), textural (Fig. S3a) and thermal (Fig. S4) characterization are shown in the SI. Concisely, the method used to precipitate MIL-100(Fe) is based on the slow reaction of Fe^{2+} and H_3BTC in water, straightforwardly giving a crystalline phase. In contrast, the synthesis of FeBTC entails the fast reaction of Fe^{3+} and H_3BTC in dioxane, thus forming an intermediate gel constituted by amorphous colloidal particles. The modus of drying the gel highly influences the characteristics of the end product. In this work, the FeBTC gel was dried in a $scCO_2$ atmosphere, yielding isometric NPs with sizes in the order of 10-20 nm (Fig. S5a). The structural disorder of this phase is reflected in the XRD pattern by strong peak widening (Fig. 3a). Nevertheless, the broad peaks at 2θ=3.9 and 11º matched the MIL-100(Fe) accumulated narrow peaks in these regions, denoting structural similarities among both trimesate MOFs.[40] The molecular structure of the semiamorphous FeBTC was analyzed by FTIR-ATR spectroscopy (Fig. 4a). The spectrum displayed the bands of iron trimesate, consisting of various sharp bands in the zone below 1300 cm^{-1}, and two sets of bands at 1622

and 1566 cm^{-1} and 1444 and 1370 cm^{-1}, corresponding to the asymmetric and symmetric stretching vibrations of the carboxylate group coordinated to iron. Regarding N_2 physisorption, FeBTC displayed a type I isotherm, with enhanced adsorption in the low pressure region, denoting intraparticle porosity provided by small mesopores accessible through micropore windows (Fig. S3b).[41]

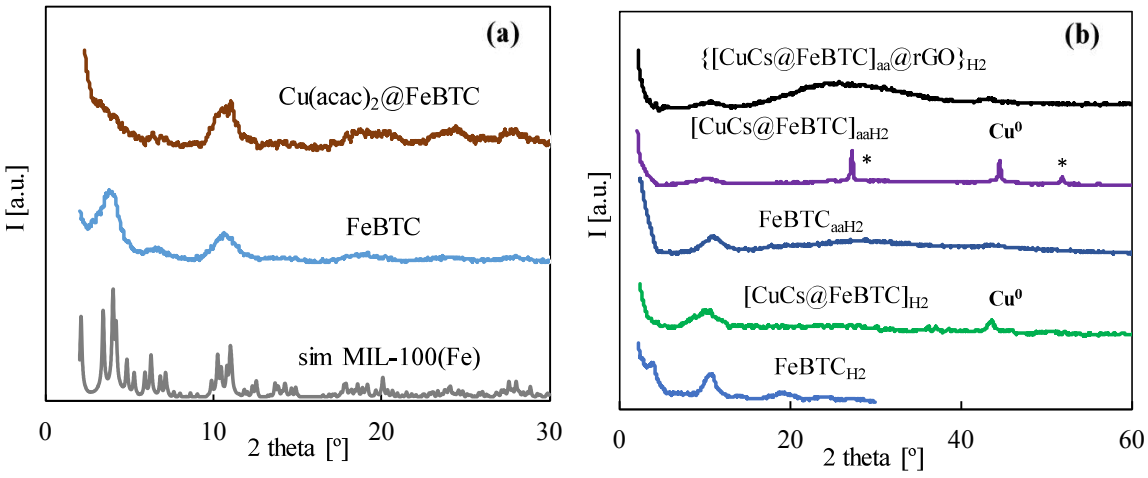

Figure 3. Powder XRD patterns of: (a) as-synthetized and $Cu(acac)_2$ impregnated FeBTC, also including the simulated MIL-100(Fe) for comparison, and (b) reduced samples (in the $[CuCs@FeBTC]_{aaH2}$ pattern, * indicates graphite peaks).

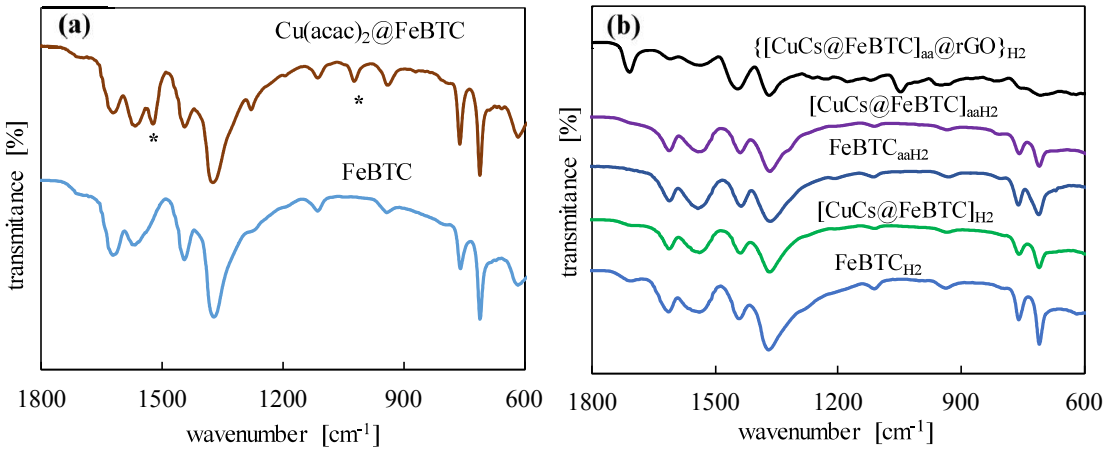

Figure 4. FTIR-ATR spectra of: (a) as-synthetized and $Cu(acac)_2$ impregnated FeBTC (in the $[CuCs@FeBTC]_{aaH2}$ spectrum, * indicates peaks for acac moiety), and (b) reduced samples.

The isotherm of synthetized FeBTC is similar to the one recorded for crystalline MIL-100(Fe) (Fig. S3a), but with reduced values of N_2 adsorption due to intrinsic defects on the framework of the semiamorphous MOF. For FeBTC, the measured apparent BET S_a was 1074 m^2g^{-1}, with a V_{mp} of 0.33 cm^3g^{-1}. The observed hysteresis at high relative pressures pointed to capillary condensation in interparticle mesopores giving a V_p of *ca.* 0.1 cm^3g^{-1}. During pyrolysis, the onset of thermal decomposition for semiamorphous FeBTC occurred at temperatures of *ca.* 290-300 ºC, whic is *ca.* 20 ºC lower than for crystalline MIL-100(Fe) (Fig. S4).

To generate the target catalyst, a precursor of the copper active units must be first incorporated into the MOF pores. Persisting on the aim of developing sustainable processes, the use of green $scCO_2$ was surveyed for the transport of the chosen precursor into the pores. Related to that, the supercritical method has important advantages, such as improved reagent diffusion into small diameter cavities, mass transport not hindered by capillary forces, and null competition between solvent and solute by the adsorption sites.[42] However, an essential prerequisite to use this method is to attain significant solubility of the precursor in the fluid under reasonable values of pressure and temperature, *e.g.*, < 250 bar and < 100 ºC. The use of low pressure values would reduce process costs, while the use of low temperatures avoids the early thermal decomposition of the precursor and/or support. In this study, the molecular precursor was searched among the organometallic copper family, since typical inorganic copper salts are all insoluble in $scCO_2$. In particular, the $Cu(acac)_2$ molecule was chosen, since it has a reasonable solubility value in $scCO_2$, in the order of *ca.* $5 \cdot 10^{-5}$ mole fraction at the selected working conditions of 200 bar and 80 ºC.[43] Besides, $Cu(acac)_2$ is an elongated molecule with approximated dimensions of 0.5 x 0.5 x 0.7 nm. Hence, this precursor has the proper size to impregnate the FeBTC cages of almost 3 nm, and also to travel through the small windows of *ca.* 1 nm connecting the mesocages. The $scCO_2$ impregnation was successfully achieved under chosen conditions, giving a $Cu(acac)_2$@FeBTC sample with metal percentages, established by

ICP-MS, in the order of 5.0 and 15 wt% for copper and iron, respectively. Considering the value measured for copper, the percentage of $Cu(acac)_2$ in the sample was estimated as 23 wt%. Despite the attained high loading, the XRD pattern did not display the intense peaks of crystallized $Cu(acac)_2$ at 2θ=11.3 and 11.7º, but only those of FeBTC (Fig. 3a). This result is characteristic of guest impregnation in confined spaces of reduced dimensions, in which crystals do not have place to grow. Guest molecules are incorporated by the phenomenon of pore filling, typically adsorbed on the pore walls in the molecular form or forming small amorphous clusters.[44] The signal at 2θ=2.9º, assigned in net FeBTC to empty mesoporous cages, almost disappears from the pattern of the impregnated sample, which is taken as an indication of high loading. This signal is assigned in the FeBTC crystal to the ordered arrangement of the nanopores. For net FeBTC, this is a sharp diffraction peak indicating empty pores in the vacuum activated MOF. The reduction in intensity of low angle peaks in nanoporous compounds has been described as an indication of reversible deformation of pore walls when they are loaded with guess molecules. The presence of $Cu(acac)_2$ in the impregnated composite was further corroborated by FTIR-ATR spectroscopy (Fig. 4a). Together with the signals of FeBTC, the spectrum exhibited two extra bands at 1520 and 1021 cm^{-1}, assigned to symmetric C=O stretching and CH_3 rocking from the acac moiety. SEM images indicated similar morphology for pristine and impregnated FeBTC (Fig. S5a,b), not revealing for the later the typical $Cu(acac)_2$ needles precipitated in $scCO_2$, contrarily to what happen for $Cu(acac)_2$@MIL-100(Fe) (Fig. S2b). The successful loading of $Cu(acac)_2$ into the pores of the semiamorphous FeBTC was corroborated by the massive volumetric decrease of N_2 physisorption at low relative pressures (Fig. S3b), giving a negligible intraparticle micropore volume, but still maintaining some interparticle mesopore volume of *ca.* 0.1 cm^3g^{-1}. At this point, it is worth mentioning that, under used experimental conditions, loading of $Cu(acac)_2$ into the pores of the studied iron trimesate MOFs was only feasible for the

semiamorphous FeBTC, and no for the crystalline MIL-100(Fe) counterpart (see SI). The reason of the different impregnation behavior was related to the affinity of the $Cu(acac)_2$ for the MOF pore walls, which is considered as the impregnation driven force. The intensity of the solute-pore wall interaction can be ascertained through the analysis of the C parameter in the BET equation inferred from the N_2 adsorption/desorption isotherm, which is exponentially related to the energy of the adsorbed solute.[45] FeBTC presents an exceptionally high value for this parameter (C=315), denoting the heterogeneity of the pore walls conditioned by a large number of defects. This value is reduced to 80 in the crystalline MIL-100(Fe), with atomically homogeneous pore walls. Hence, in the semiamorphous FeBTC, strong electrostatic interactions of $Cu(acac)_2$ on the high-energy surface defects and Brönsted acid sites are favored *vs*. solvation by $scCO_2$, while in the crystalline MIL-100(Fe) solute adsorption is energetically discarded.[46] The semiamorphous character of FeBTC is clearly an advantage for impregnation with the catalyst precursor.

3.2. Catalyst activation by reduction

The $Cu(acac)_2$@FeBTC precursor needs to be activated by reduction to obtain the Cu^0/Cu^+ phase catalytically active in the CO_2 hydrogenation reaction. In this work, this is attained by the *in situ* growth of reduced copper clusters (CuCs, *e.g.*, Cu^0/CuO) into the constrained void space of the FeBTC pores, giving place to structures of the CuCs@FeBTC type. Two different routes were used for reduction, the first one performed under relatively mild conditions by using H_2 at 260-300 ºC, and the second at harsh conditions involving, initially, a treatment with ascorbic acid and, then, with H_2 at 300 ºC. When using the one step reduction route, based exclusively on H_2 as the reductant, significant variations between results obtained at 260 and 300 ºC were not observed. Hence, described experiments were those carried out preferably at 260 ºC, chosen as a temperature that would largely avoid the collapse of the framework structure at the surface. Instead, for the two steps ascorbic acid/H_2 reduction process, the

catalytic production of MeOH was readily enhanced at 300 ºC, choosing this temperature for further reactions, even further amorphization of the FeBTC surface was likely to occur. In both cases, H_2 reduction is conducted *in situ* in the reactor used for catalysis, and is performed just before the CO_2 hydrogenation reaction. Therefore, samples characterization is performed in the spent catalysts.

3.2.1. Reduction with H_2

To analyze the stability of the $Cu(acac)_2$@FeBTC components under H_2 reduction conditions, separate tests were performed for pristine $Cu(acac)_2$ and FeBTC. Pristine $Cu(acac)_2$ particles, used as-received, were not stable when subjected to H_2 reduction at 260 ºC. XRD analysis indicated its decomposition in mainly Cu^0 (bands at 2θ=43.1 and 50.3º), mixed with some Cu_2O (bands at 2θ=36.4º and 42.3°), not depicting neither the intense bands of $Cu(acac)_2$ (at 2θ=11.4 and 11.7º) nor those of CuO (at 2θ=35.5 and 38.6º) (Fig. S6). On the contrary, XRD (Fig. 3b) and FTIR-ATR (Fig. 4b) structural analysis of the obtained $FeBTC_{H2}$ sample showed a high degree of framework stability under these reduction conditions. N_2 adsorption at low temperature indicates that the reduced sample was still porous, with a significant V_{mp} of 0.08 cm^3g^{-1} and a V_p of *ca.* 0.1 cm^3g^{-1} (Fig. S7a).

The thermal reduction with H_2 of $Cu(acac)_2$@FeBTC lead to $[CuCs@FeBTC]_{H2}$. Structurally, this sample displayed the XRD peaks of FeBTC, but with an additional signal at 2θ=43.3º indicating the presence of Cu^0 NPs, with a diameter of 14 nm estimated by the Scherrer equation (Fig. 3b). This cooper phase is ascribed to particles located outside the FeBTC channels, with a maximum diameter of 3 nm. Actually, pore-confined entities should be too small to be detected as a crystalline compound by routine XRD analysis. The acetylacetonate moiety was not visible in the FTIR-ATR spectrum of the composite, which was similar to that of FeBTC (Fig. 4b). The percentile amount of metals in the spent catalyst was quantified by ICP-MS as 9.5:34 wt% for Cu:Fe, with a Cu/Fe ratio of 0.28, similar to that measured for the

precursor $Cu(acac)_2$@FeBTC of 0.31. The slight reduction in the Cu percentage can be explained by the evaporation of some $Cu(acac)_2$ molecules during reduction. The elimination of acac moieties from the non-porous $Cu(acac)_2$@FeBTC did not open the pores of resulting $[CuCs@FeBTC]_{H2}$, which are now filled with copper clusters (Fig. S7a). The EDS elemental mapping of Fe and Cu on a nanometric section of the spent catalysts indicates that both metals were homogeneously distributed (Fig. 5). In the copper map, few dense spots can be discriminated, assigned to some NPs located outside of the FeBTC pores. These spots are believed to be the origin of the Cu^0 XRD peak at 2θ=43.3º mentioned above (Fig. 3b). These metal copper particles would not be effective in the studied catalytic process due to both, their relatively large size and low quantity.

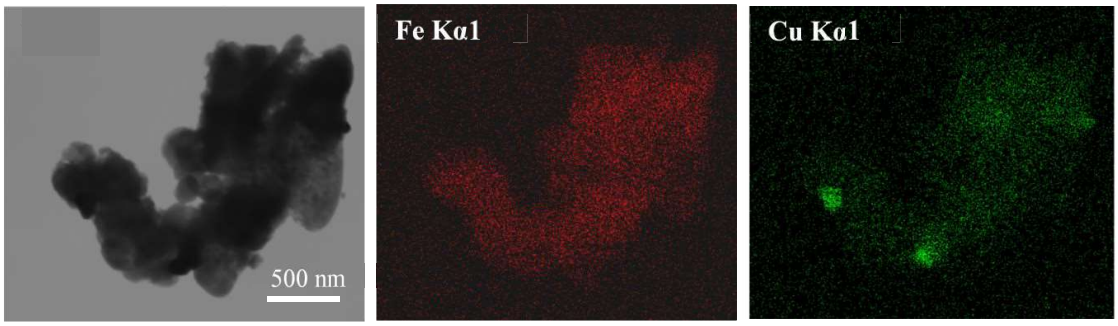

Figure 5. STEM image and metal EDS maps of the $[CuCs@FeBTC]_{H2}$ composite, showing iron (red) and copper (green) distributions.

The $[CuCs@FeBTC]_{H2}$ composite was further studied by XPS (Table S1 and Fig. S8,S9). Comprehensive data discussion is presented in the SI. Succinctly, the analysis indicates excess of oxygen and carbon, since the O/Fe and C/Fe atomic ratio have values of 7.5 and 12, respectively, higher than the ratios for stoichiometric FeBTC ($C_9H_3FeO_6$, with O/Fe=6 and C/Fe=9). The C1s region shows the typical profile described for trimesic acid units (Fig. S8a,b),[47] but with an area ratio C=O to C-O of *ca.* 2, while the ratio expected for stoichiometric FeBTC is 1. In the O1s region a large excess of C=O is also observed. The slight O excess, and some C excess, can be ascribed to residual acetylacetonate groups not totally reduced on the

spent catalyst or even derivatives of this moiety, *e.g.*, acetone or acetic acid.[48] Further carbon excess might be due to the formation of coke, carbide or graphite deposits during the CO_2 hydrogenation reaction. Regarding the Fe2p region, peaks of Fe^{2+}/Fe^{3+} (59 at%) and Fe^{3+} (41 at%) species are present. Finally, peaks in the Cu2p region are assigned to Cu^{+}/Cu^{0} (48 at%) and Cu^{2+} (52 at%) species, with a mixture of oxidation states in the sample (Fig. S9). The Fe:Cu metallic composition on the surface stablished by XPS is 3.8:1, close to the 4:1 ratio measured by ICP-MS for the bulk. These similar values prospect a homogenous distribution of the metals on the composite, indicating a low percentage of Cu^{0} NPs deposited outside the MOF pores, as already observed in the EDS elemental mapping (Fig. 5).

3.2.2. Reduction with ascorbic acid plus H_2

With the objective of increasing the copper phase reduction grade, the $Cu(acac)_2$@FeBTC precursor was subjected to a harsh reduction process, starting with ascorbic acid in liquid phase and finalizing with H_2 gas at 300 ºC. Ascorbic acid is considered an environmentally friendly and non-toxic reductant, highly efficient for the removal of oxygen groups and with low risk of introducing heteroatoms in the reaction products.[49] To analyze the stability of the MOF framework under these conditions, net FeBTC was first treated following a similar double reduction liquid/gas method. The structural analysis of the $FeBTC_{aaH2}$ sample indicates that the principal characteristics of the MOF framework were preserved. Thus, the framework peak at 2θ *ca.* 11º and the carboxylate functional groups in the 1700-1200 cm^{-1} region were discernible in the respective XRD (Fig. 3b) and FTIR-ATR (Fig. 4b) spectra. Contrarily to $FeBTC_{H2}$ (Fig. S7a), N_2 adsorption analysis showed negligible microporosity for $FeBTC_{aaH2}$ (Fig. S7b), likely due to the collapse of the MOF framework on the surface, and consequent blocking of pore entrance. Similar to $FeBTC_{aaH2}$ sample, the double reduction of $Cu(acac)_2$@FeBTC produced a $[CuCs@FeBTC]_{aaH2}$ spent catalyst displaying in the XRD pattern the wide peak of the semiamorphous FeBTC at 2θ *ca.* 11º (Fig. 3b). In this spectrum, the peak at 2θ=43.3º was

assigned to Cu^0 NPs, with a Scherrer estimated crystal size of *ca*. 30 nm. A new intense band arising at 2θ=27.2º, together with the small peak at 2θ=54.5º, were attributed to graphite formation due to partial decomposition of the organic components in the composite and deposits during the hydrogenation reaction. FeBTC carboxylic functionalities were still evident in the FTIR-ATR spectrum (Fig. 4b). In regard of N_2 physisorption, the sample showed negligible microporosity (Fig. S7b). Elemental mapping of $[CuCs@FeBTC]_{aaH2}$, performed on a large section of the sample using a SEM microscope (Fig. 6), indicated homogeneous distribution of Cu and Fe, with some dense spots on the Cu map attributed to the large Cu^0 NPs already observed in the XRD pattern.

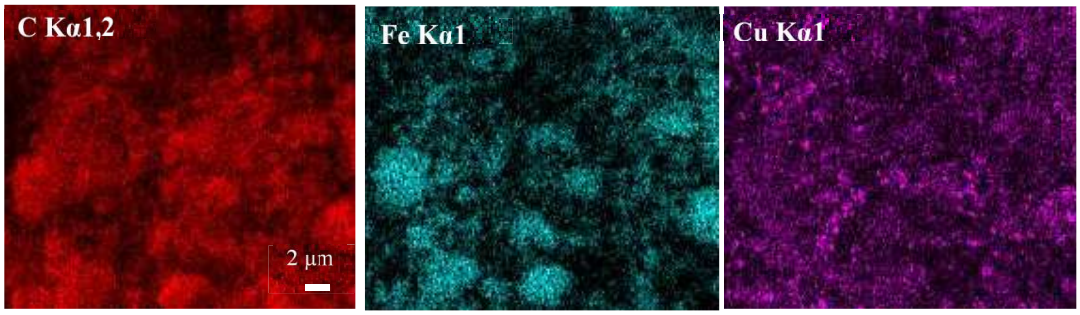

Figure 6. EDS distributions of carbon (red), iron (blue) and copper (purple) in a SEM image.

$FeBTC_{aaH2}$ and $[CuCs@FeBTC]_{aaH2}$ were analyzed by XPS, displaying both samples a complex behavior that is discussed in the SI (Table S1 and Figs. S10-S14). Briefly, measured C/Fe relative amounts on the surface were certainly higher than that corresponding to stoichiometric FeBTC, which is ascribed to carbon deposits formed during the hydrogenation reaction of CO_2. Unlike for the former $[CuCs@FeBTC]_{H2}$, the C1s and O1s regions for these samples were not consistent with the typical profile of trimesic acid units in the FeBTC MOF in regard of binding energies and mass balance of C and O species. In particular, for both the main C=O band constitutes *ca.* 90 % of the O1s area, and appeared at a binding energy lower that 530 eV, well below values known for common oxygenated carbon species.[50] Moreover,

peaks in the Fe2p region indicated that iron was in a highly reduced state, involving iron carbides (*e.g.*, Fe_5C_2 and Fe_7C_3) and oxygen-deficient FeO, with only a small fraction of Fe^{+3} oxides. For the $[CuCs@FeBTC]_{aaH2}$ sample, the Cu2p region displayed peaks at binding energies typical of highly reduced species, with surface values of 67 at% Cu^+ and 33 at% Cu^0. Hence, the double ascorbic acid/H_2 reduction route was harsh enough to achieve the utterly reduction of surface copper. Likely, the concomitant reduction of iron has as a consequence the collapse of the FeBTC network on the surface, as already rationalized by the null adsorption of N_2. The main conclusion from the XPS analysis is that the surface catalytic layer must be extremely thin, with a thickness below ~5 nm. The oxygen species prevailing in this thin layer might be either adsorbed oxygen[51] or nucleophilic oxygen atoms located at the prismatic edges of stacked graphene sheets.[52]

3.2.2. Reduction with ascorbic acid plus H_2 and addition to GO support

In a previous work, it has been demonstrated that the use of rGO as a support improves the catalytic behavior of CuZnO NPs in the CO_2 hydrogenation reaction.[17] This approach was tested in this work by dispersing the CuCs@FeBTC catalyst on this support. The target composition was *ca.* 9:1 for [CuCs@FeBTC]:rGO, *i.e.*, highly concentrated in the active catalyst. The double reduction route was applied in two steps. In the first one, the precursor $Cu(acac)_2$@FeBTC was reduced with ascorbic acid. SEM images indicated that the obtained $[CuCs@FeBTC]_{aa}$ sample was forming aggregates of 2-5 μm (Fig. 7a). The $[CuCs@FeBTC]_{aa}$ NPs were spread all over the aerogel, constituting the discontinuous phase in the $[CuCs@FeBTC]_{aa}$@GO composite and forming aggregates of less than 1 μm (Fig. 7b). In the second reduction step, the composite was treated with H_2 at 260 ºC to obtain the $\{[CuCs@FeBTC]_{aa}@rGO\}_{H2}$ sample. The ascorbic acid reduction was not applied to the system involving GO because this reductant has the disadvantage of the irreversible formation of graphene agglomerates that are not useful as a support for the NPs. For the double reduced

sample, the presence of the typical FeBTC XRD peak at 2θ *ca.* 11º indicates the preservation of certain integrity of the MOF framework (Fig. 3b). These peak could be also contributed by non-reduced GO, described by a single wide peak at 2θ *ca.* 11.1°, but this assignment is unlikely because of the used harsh reduction route. In fact, the reduction of GO to rGO is confirmed by the wide band emerging at 2θ *ca.* 25°.[53] The FTIR-ATR spectrum displayed the main functional groups of FeBTC, as well as an extra band at 1730 cm^{-1} assigned to >C=O functionalities, typically present in the edges of rGO flakes (Fig. 4b).[35] The morphology of $\{[CuCs@FeBTC]_{aa}@rGO\}_{H2}$ (Fig. 7c) was similar to that of $[CuCs@FeBTC]_{aa}@GO$ (Fig. 7b). Regarding N_2 physisorption, this sample shows a type IV isotherm with hysteresis at medium-high relative pressures, indicating significant mesoporosity (V_p *ca.* 0.3 cm^3g^{-1}) given by the aerogel support (Fig. S7b).

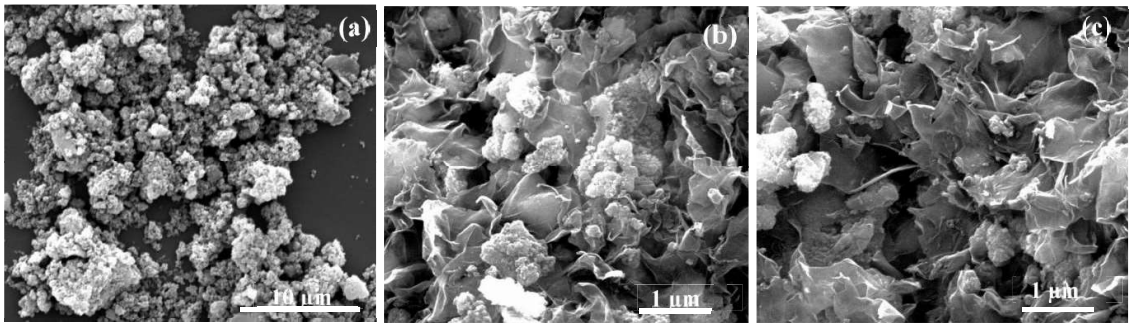

Figure 7. SEM images of: (a) $[CuCs@FeBTC]_{aa}$, (b) $[CuCs@FeBTC]_{aa}@GO$, and (c) $\{[CuCs@FeBTC]_{aa}@rGO\}_{H2}$.

3.3. Effectiveness in the CO_2 hydrogenation reaction

3.3.1. $[CuCs@FeBTC]_{H2}$ catalyst

In the CO_2 hydrogenation reaction, the use of H_2 as the reductant would have relevant operational advantages, since consecutive reduction and CO_2 hydrogenation can be performed in a single high-pressure holder, simply by switching the gas inlet, without any transitional manipulation of the sample (Fig. 1c). Therefore, first trials in this work were performed by thermal H_2 reduction of the precursor $Cu(acac)_2@FeBTC$. In the studied reaction temperature

interval of 180 to 260 ºC, $[CuCs@FeBTC]_{H2}$ produced MeOH and CH_4 in appreciable quantities (Fig. 8a), with MeOH/CH_4 selectivity values in the order of 70 wt% (Fig. 8d). The source of methane is uncertain. Indeed, the composition of the H_2:CO_2 feeding gas mixture, with a 3:1 molar ratio, was selected anticipating the prevalence of MeOH as the end product ($CO_2 + 3H_2 \rightarrow CH_3OH + H_2O$), while the formation of CH_4 is optimized at a 4:1 ratio ($CO_2 + 4H_2 \rightarrow CH_4 + 2H_2O$). In the first stages of reaction, the possibility of being the hydrogenolysis of residual acetyl acetonate the source of methane was considered.[54] However, a blank performed with pristine $Cu(acac)_2$ reduced in situ with H_2, as described in section 3.2.1, did not showed any catalytic activity under studied CO_2 hydrogenation conditions, neither regarding CH_4 nor MeOH (Table 1), thus discarding this hypothesis. Actually, Cu^0 NPs prepared in this way grow to sizes of more than 10 nm, which would result in a very low catalytically active surface area. Some authors have described the blending of Cu/Cu^+ and Fe^{+2}/Fe^{+3} to constitute a catalyst with efficiency in the formation of methane.[55] The option of being reduced FeBTC the catalysts promoting methane formation was tested in a separate hydrogenation experiment involving exclusively the MOF. The $FeBTC_{H2}$ sample showed some measurable catalytic activity itself, giving MeOH STY values of *ca.* 0.1 $mg_{MeOH}g_{FeBTC}^{-1}h^{-1}$ at 260 ºC, but negligible CH_4 production. It is worth pointing that, under similar working conditions, the catalytic activity of crystalline $MIL\text{-}100(Fe)_{H2}$ was negligible regarding both MeOH and CH_4 production. Such disparities on the catalytic behavior of both trimesic iron MOFs are related to the different structural characteristics. Likely, defects in FeBTC entail a large number of bare coordination sites in the Fe^{3+}/Fe^{2+} nodes, which might promote the dissociation of some H_2.[56] The importance of defects in the structure of this MOF has been already illustrated in acid catalyzed acetalization and epoxide ring-opening reactions.[57,58]

For the $[CuCs@FeBTC]_{H2}$ catalyst, the efficiency of the CO_2 hydrogenation reaction can be considered as low, with CO_2 conversion values in the order of 0.3 wt%, which, together with a

reduced MeOH/(CO+CH_4) selectivity of only 11 wt%, end in reduced STY_{MeOH} of 11 $mg_{MeOH}g_{Cu}^{-1}h^{-1}$. The STY_{CH4} was 5 $mg_{CH4}g_{Cu}^{-1}h^{-1}$, half of the STY_{MeOH}. Since the XPS estimated surface composition was 47 at% Fe^{2+}/Fe^{3+}, 32 at% Fe^{3+}, 11 at% Cu^{2+} and only 10 at% Cu^{+}/Cu^{0}, the low efficacy of this catalyst is related to the moderate amount of reduced copper found on the sample surface. Even though pristine $Cu(acac)_2$ could be totally reduced to Cu^{+}/Cu^{0} phases using H_2 flow at 260 ºC (Fig. S6), the confinement of the precursor into the MOF pores hinders their extensive reduction under similar experimental conditions, likely due to diffusion restriction (H_2 in and acac out of pores). It should be pointed out that the catalytic activity of the material obtained from the reduction of net $Cu(acac)_2$ was negligible, indicating extensive growth and sintering of Cu^0 particles. Actually, the main reason behind impregnating the copper metal precursor into the pores of FeBTC was to avoid these undesired processes of growth, sintering and crystal ripening during reduction to CuCs and further catalytic reaction at high temperature.

3.3.2. $[CuCs@FeBTC]_{aaH2}$ catalyst

With the objective of designing a more efficient catalyst by increasing the number of surface active Cu^0/Cu^+ centers, the use of a strong reductant for the confined $Cu(acac)_2$ was considered. For this, $Cu(acac)_2$@FeBTC was first treated with ascorbic acid, a soft-chemistry reductant. However, the resulting $[CuCs@FeBTC]_{aa}$ samples did not improve the catalytic performance in comparison to $[CuCs@FeBTC]_{H2}$. Further reduction was then established by processing the $[CuCs@FeBTC]_{aa}$ sample with H_2 at 300 ºC. Following the two-step reduction route in the $[CuCs@FeBTC]_{aaH2}$ sample, CO_2 conversion values were multiplied by a factor of 10 with respect to $[CuCs@FeBTC]_{H2}$, reaching 3.1 wt% at 260 ºC, which can be increased up to *ca.* 7 wt% at 300 ºC. However, the main reaction product at these high temperatures was CH_4, with a STY_{CH4} of 67 $mg_{CH4}g_{Cu}^{-1}h^{-1}$ at 260 ºC (156 $mg_{CH4}g_{Cu}^{-1}h^{-1}$ at 300 ºC), instead of MeOH, with a STY_{MeOH} of *ca.* 20 $mg_{MeOH}g_{Cu}^{-1}h^{-1}$ at both mentioned temperatures (Fig. 8b). The

(MeOH+CH_4)/CO selectivity value was *ca*. 30 wt% (Fig. 8e), but with a MeOH/(CH_4+CO) selectivity of only 6 wt%. The main surface particularity found in XPS for $[CuCs@FeBTC]_{aaH2}$ is that Fe^{3+} and Cu^{2+} were highly reduced to Fe^{2+}/Fe^0 and Cu^+/Cu^0 phases, respectively. Thus, in general lines, the enhanced catalytic activity of $[CuCs@FeBTC]_{aaH2}$ with respect to $[CuCs@FeBTC]_{H2}$ can be explained by an increased number of reduced copper species on the surface. Nevertheless, the influence of reduced iron species must be also taken into account, particularly to explain the increased amount of produced CH_4. This reasoning was proved by synthetizing net $FeBTC_{aaH2}$ catalyst, which displayed more competent values than $FeBTC_{H2}$. At 260 ºC, three and four-fold increase in STY_{MeOH} (0.63 $mg_{MeOH}g_{FeBTC}^{-1}h^{-1}$) and STY_{CH4} (0.43 $mg_{CH4}g_{FeBTC}^{-1}h^{-1}$) were observed for $FeBTC_{aaH2}$. In samples treated with ascorbic acid, *e.g.,* $FeBTC_{aaH2}$ and $[CuCs@FeBTC]_{aaH2}$, XPS indicates the formation of iron carbides (Fe_5C_2 and Fe_7C_3) and oxygen-deficient FeO that must have some catalytic activity. These surface species are consistent with the reported mechanism of CO_2 hydrogenation with iron, in which cationic surface iron is first reduced to iron NPs, and then carburized with dissociated carbon species ($CO_2 \rightarrow CO \rightarrow C$) to form an amorphous iron carbide layer that is the active phase for the hydrogenation of CO (reduced CO_2).[59] The catalytic activity may also arise from the nucleophilic oxygen atoms observed by XPS (see SI), and located at the prismatic edges of stacked graphite sheets.[50,51] Graphitic forms of carbon are known to have interesting potential for catalysis in reactions of hydrogenation, oxidation, etc.[52] Although CH_4 is considered less valuable as end product than MeOH, it can be used as an intermediate specie, since it has been shown that secondary processes of CO and CH_4 to form chemicals and fuels can increase the overall CO_2 hydrogenation yield through a less energy-intensive pathway.[60]

3.3.3. $\{[CuCs@FeBTC]_{aa}@rGO\}_{H2}$ catalyst

Two factors have been recognized to limit the catalytic activity of CuCs@FeBTC samples. First, the encountered difficulties in reducing the confined $Cu(acac)_2$ precursor, shortcoming

that was solved by using a double reduction route. Second, restricted diffusion into the channels of FeBTC, when it is charged with CuCs species, which limit the mass transport of reagents (H_2 and CO_2) to the catalytically active sites, as well as products (MeOH, CH_4, CO and H_2O) out of the pores. In an attempt of reducing diffusion drawbacks, the composite catalyst was dispersed on a substrate. A GO aerogel, with demonstrated advantages in the hydrogenation reaction, has been selected for this purpose.[17] CO_2 hydrogenation tests performed with $\{[CuCs@FeBTC]_{aa}@rGO\}_{H2}$ indicate that the incorporation of GO results in a significant improvement of the catalytic performance in regard of MeOH production rate, concomitant with null production of CH_4 (Fig. 8c). This increase in methanol yield is observed even the total CO_2 conversion has a value of only 0.3-0.5 wt%, because the selectivity for the production of the alcohol is near 100 wt% at all the studied temperatures (Fig. 8f). As a consequence, a STY_{MeOH} value of 86 $mg_{MeOH}g_{Cu}^{-1}h^{-1}$ was reached at 260 ºC, which represents a four-fold increase with respect to $[CuCs@FeBTC]_{aaH2}$ lacking of GO support. The increase in MeOH selectivity has been attributed to the hydrophobic nature of rGO, which inhibits water adsorption and protects the deactivation of the active Cu^+/Cu^0 metal centers, as it was demonstrated in a previous work involving Cu/ZnO@rGO.[17]

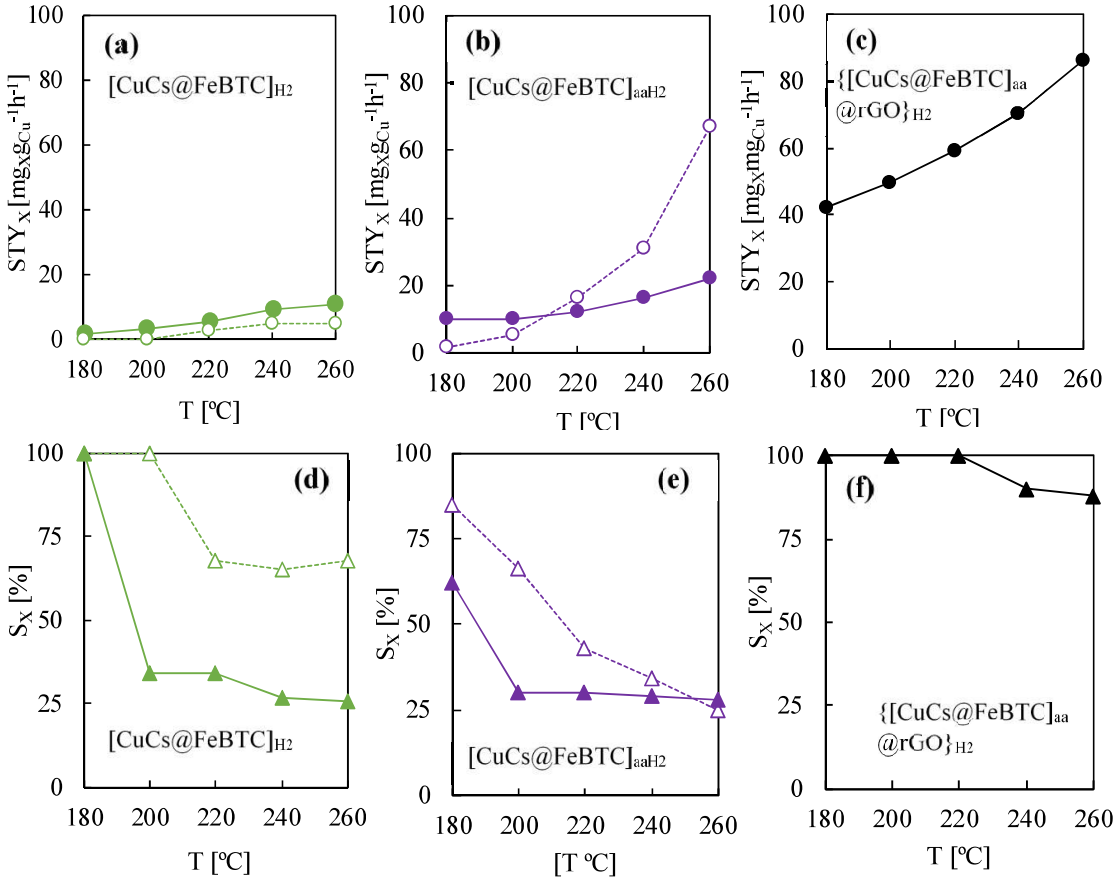

Figure 8. Catalytic data obtained for the different samples as a function of the reaction temperature at 10 bar: (a,d) $[CuCs@FeBTC]_{H2}$, (b,e) $[CuCs@FeBTC]_{aaH2}$, and (c,f) $\{[CuCs@FeBTC]_{aa}@rGO\}_{H2}$. In (a,b,c) STY_X represents STY_{MeOH} (solid line) or STY_{CH4} (dotted line). In (d,e,f) Sx represents $S_{(MeOH+CH4)/CO}$ (solid line) or $S_{MeOH/CH4}$ (dotted line).

3.3.4. Comparison to literature data

To analyze the effectiveness of the designed catalysts, MeOH yield obtained by the synthetized catalyst was compared to that of the typical CuZnO catalyst used for MeOH production in the CO_2 hydrogenation reaction, and to other CuZnO-based systems involving different porous supports. Results obtained in this work with the different analyzed samples are summarized in Table 1.

Table 1. Catalytic data (at 260 ºC and 10 bar) obtained in this work for the prepared samples.

Sample	STY_{MeOH} $[mg_{MeOH}g_{MOF}^{-1}h^{-1}]$	STY_{CH4} $[mg_{CH4}g_{MOF}^{-1}h^{-1}]$	$S_{MeOH/CO}$	$S_{CH4/CO}$
$[Cu(acac)2]_{H2}$	0	0	--	--
MIL-100(Fe)	0	0	25	--
$FeBTC_{H2}$	0.1	0	2	--
$FeBTC_{aaH2}$	0.63	0.43	6.5	3.6
	$[mg_{MeOH}g_{Cu}^{-1}h^{-1}]$	$[mg_{CH4}g_{Cu}^{-1}h^{-1}]$		
[CuCs@FeBTC]H2	11	5	11	
$[CuCs@FeBTC]_{aaH2}$	20	67	5	17
$\{[CuCs@FeBTC]_{aa}@rGO\}_{H2}$	86	0	92	--

Taking into account that catalytic tests in this work were performed at standard temperatures, but at a pressure of only 10 bar, results are compared to that obtained with catalyst tested under similar conditions. At 260 ºC and 10 bar, net CuZnO NPs provided STY_{MeOH} values below 5 $mg_{MeOH}g_{Cu}^{-1}h^{-1}$, while applying the NPs to porous supports, such as activated carbon, zeolite or graphene oxide, gave values in the interval of 15-23 $mg_{MeOH}g_{Cu}^{-1}h^{-1}$.[17,18,61] These MeOH production rates are in the range of the values measured in this work for the $[CuCs@FeBTC]_{aaH2}$ sample, with 22 $mg_{MeOH}g_{Cu}^{-1}h^{-1}$. Published Cu-MOF systems of the core-shell type, involving ZIF-8, MIL-100, UiO-66, reported MeOH production rates significantly lower than samples in this work, in the order of 1-12 $mg_{MeOH}g_{Cu}^{-1}h^{-1}$, although data were obtained at only 2 bar.[62] In this work, the insertion of GO as a support for the CuCs@FeBTC NPs produced the best results with a STY_{MeOH} of 86 $mg_{MeOH}g_{Cu}^{-1}h^{-1}$, which represent a three- to four-fold increase respect to published values, with methanol selectivity values of nearly 100 wt% and null production of methane.

4. Conclusions

The direct use of MOFs composite in the catalytic transformation of CO_2 into methane and/or methanol is presented. In the overall process, green chemistry concepts are applied to the choice of catalyst, substrate, solvents and reducing agents. Relevance of using semiamorphous *vs*. crystalline MOFs is proved trough the use of iron trimesate MOFs: FeBTC *vs.* MIL-100(Fe). Semiamorphous FeBTC is synthetized through a less energy intensive pathway in sustainable solvents, not requiring extensive post-processing like the crystalline counterpart, moreover leading to enhance catalytic activity. Graphene oxide is used to further increase catalysts performance. Precursor composite catalysts of the type $[Cu^{2+}@FeBTC]@GO$ are synthesized using green methods involving mainly green supercritical CO_2 for the nanostructuration. In this respect, this work opens the spectrum of possibilities for the $scCO_2$ synthesis of composites involving metal clusters into MOF pores by selecting adequately the organometallic precursors. The synthesis continues with catalyst reduction to obtain [CuCs@FeBTC]@rGO. However, to preserve the integrity of the MOF, typical thermal reduction with H_2 could not be performed at the temperature values necessary for an efficient conversion of Cu^{2+} to Cu^{+}/Cu^{0}, which are described to be in the order of 320-350 ºC for different substrates. Ascorbic acid, a green and inexpensive reductant used in water, is selected to increase copper phase reduction, thus avoiding the use of toxic hydrazine or sodium borohydride, which causes the accumulation of waste harmful to the environment. The basic concept for all the studied systems is to disperse CuCs into the porous structure of FeBTC, thus confining the clusters into the mesoporous cages that physically hinders the growth and aggregation of the copper species during reduction and catalysis. From the three studied catalysts, $[CuCs@FeBTC]_{H2}$ gives a low CO_2 conversion with minimal production rates of both MeOH and CH_4; $[CuCs@FeBTC]_{aaH2}$ leads to relatively high CO_2 conversion values and increased CH_4 yield; and $\{[CuCs@FeBTC]_{aa}@rGO\}_{H2}$ produces large amounts of MeOH even at low CO_2 conversion. The $[CuCs@FeBTC]_{aaH2}$ composite has

the particularity of producing large amounts of CH_4 without the use of noble metals, which was favored by increasing the temperature, reaching a STY_{CH4} value of 67 $mg_{CH4}g_{Cu}^{-1}h^{-1}$ at 260 ºC. For this sample, CO_2 conversion reached a value of 3 wt% at 260 ºC, which is increased up to 7 wt% at 300 ºC, values which are rarely reached at the working H_2 pressure of only 10 bar. Even the high yield of CH_4 attained by sample $[CuCs@FeBTC]_{aaH2}$ could have some industrial interest, the main focus of the CO_2 hydrogenation reaction is in producing MeOH. For the studied catalysts, values of 11, 22 and 86 $mg_{MeOH}g_{Cu}^{-1}h^{-1}$ were reached at 260 ºC for $[CuCs@FeBTC]_{H2}$, $[CuCs@FeBTC]_{aaH2}$ and $\{[CuCs@FeBTC]_{aa}@rGO\}_{H2}$, respectively. With difference, sample $\{[CuCs@FeBTC]_{aa}@rGO\}_{H2}$ exhibited the highest STY_{MeOH} value, producing large amounts of methanol without the incorporation of ZnO species. This sample has the additional advantage of presenting MeOH selectivity values of nearly 100 wt% at the high temperatures necessary for CO_2 conversion. Hence, the low reaction pressure used, a detrimental factor for total CO_2 conversion, is compensated with improved MeOH selectivity at high temperature. This key outcome implies that by using rGO in the sample, the formation of CO and CH_4 was inhibited, which is one of the most important parameters in industrial-scale processes, saving important separation costs of CO/CH_4 from unconverted and recycled feed gas (CO_2/H_2).

Acknowledgments

This work was supported by the Spanish Ministry of Science and Innovation through the Severo Ochoa Program for Centers of Excellence (CEX2019-000917-S), the Spanish National Plan of Research with project PID2020-115631GB-I00 and Ecological Transition and Digital Transition Projects TED2021-1298378-C41 and TED2021-130407B-I00. A.M.L., C.D. and M.K. acknowledge the finantial support of the CSIC platform SusPlast 20219PT059. G. Marbán acknowledges the financial support provided by Principado de Asturias

(IDI/2021/000096). A. A. Markeb is the recipient of a postdoctoral fellowship from the Spanish Ministerio de Universidades, María Zambrano ID 715364.

References

1. B. Ekwurzel, J. Boneham, M.W. Dalton, R. Heede, R.J. Mera, M.R. Allen, P.C. Frumho, The rise in global atmospheric CO_2, surface temperature, and sea level from emissions traced to major carbon producers, Climatic Change 144 (2017) 579–590.
2. A. Bastas, K. Liyanage. Setting a framework for organisational sustainable development. Sustain. Prod. Consum. 20 (2019) 207-229.
3. A. Moldavska, W. Torgeir, The concept of sustainable manufacturing and its definitions: A content-analysis based literature review, J. Cleaner Prod. 166 (2017) 744-755.
4. N. Winterton, The green solvent: A critical perspective, Clean Tech. Env. Policy 23 (2021) 2499-2522.
5. T. Welton, Solvents and sustainable chemistry, Proc. R. Soc. A 471 (2015) 20150502.
6. C. Domingo, P. Subra-Paternault (Eds.), Supercritical Fluid Nanotechnology: Advances and Applications in Composites and Hybrid Nanomaterials, Pan Stanford, Singapore (2015).
7. P.G. Jessop, Searching for green solvents, Green Chem. 13 (2011) 1391−1398.
8. M. Aresta, A. Dibenedetto, A. Angelini, The changing paradigm in CO_2 utilization, J. CO_2 Utiliz. 3 (2013) 65-73.
9. F. Schorn, J.L. Breuer, R.C. Samsun, T. Schnorbus, B. Heuser, R. Peters, D. Stolten, Methanol as a renewable energy carrier: An assessment of production and transportation costs for selected global locations, Adv. App. Energy 3 (2021) 100050.
10. W. Liu, F. Wen, Y. Xue, Power-to-gas technology in energy systems: current status and prospects of potential operation strategies, J. Modern Power Sys. Clean Energy 5 (2017) 439-450.
11. A.Y. Li, A. Moores, Carbonyl Reduction and Biomass: A case study of sustainable catalysis, ACS Sustainable Chem. Eng. 7 (2019) 10182−10197.
12. P. Gao, L. Zhang, S. Li, Z. Zhou, Y. Sun, Novel heterogeneous catalysts for CO_2 hydrogenation to liquid fuels, ACS Cent. Sci. 6 (2020) 1657-1670.
13. W. Li, H. Wang, X. Jiang, J. Zhu, Z. Liu, X. Guo, C. Son, A short review of recent advances in CO_2 hydrogenation to hydrocarbons over heterogeneous catalysts, RSC Adv. 8 (2018) 7651-7669.
14. E. Furimsky, CO_2 Hydrogenation to methanol and methane over carbon-supported catalysts, Ind. Eng. Chem. Res. 59 (2020) 15393-15423.
15. A. Modak, A. Ghosh, A. Bhaumik, B. Chowdhury, CO_2 hydrogenation over functional nanoporous polymers and metal-organic frameworks, Adv. Coll. Interf. Sci 290 (2021) 102349.
16. G. Prieto, J. Zečević, H. Friedrich, K.P. de Jong, P.E. de Jongh, Towards stable catalysts by controlling collective properties of supported metal nanoparticles, Nat. Mater. 12 (2013) 34-39.

17. M. Kubovics, A. Trigo, A. Sánchez, G. Marbán, A. Borrás, J. Moral-Vico, A.M. López-Periago, C. Domingo, Role of graphene oxide aerogel support on the CuZnO catalytic activity: Enhancing methanol selectivity in the hydrogenation reaction of CO_2, ChemCatChem 14 (2022) e202200607.
18. A. Carrasco-García, Javier Moral-Vico, A.A. Markeb, A. Sánchez, Conversion of carbon dioxide into methanol using Cu–Zn nanostructured materials as catalysts, Nanomaterials 12 (2022) 999.
19. Q. Zhang, S. Wang, M. Dong, W. Fan, CO_2 hydrogenation on metal-organic frameworks-based catalysts: A mini review, Front. Chem. 10 (2022) 956223.
20. Q. Yan, X. Wu, H. Jiang, H. Wang, F. Xu, H. Li, H. Zhang, S. Yang, Transition metals-catalyzed amination of biomass feedstocks for sustainable construction of N-heterocycles, Coord. Chem. Reviews 502 (2024) 215622.
21. H. Jiang, X. Wu, H. Zhang, Q. Yan, H. Li, T. Ma, S. Yang, Toward effective electrocatalytic C–N coupling for the synthesis of organic nitrogenous compounds using CO_2 and biomass as carbon sources, SusMat. 3 (2023) 781-820.
22. D. Yang, B.C. Gates, Catalysis by metal organic frameworks: perspective and suggestions for future research, ACS Cat. 9 (2019) 1779-1798.
23. A. Corma, H. García, F.X. Llabrés i Xamena, Engineering metal organic frameworks for heterogeneous catalysis, Chem. Rev. 110 (2010) 4606-4655.
24. H. Kima, C.S. Hong, MOF-74-type frameworks: tunable pore environment and functionality through metal and ligand modification, CrystEngComm 23 (2021) 1377-1387.
25. D. Pattappan, S. Vargheese, K.V. Kavya, R.T.R. Kumar, Y. Haldorai, Metal-organic frameworks with different oxidation states of metal nodes and aminoterephthalic acid ligand for degradation of Rhodamine B under solar light, Chemosphere 286 (2022) 131726.
26. B. Li, K. Leng, Y. Zhang, J.J. Dynes, J. Wang, Y. Hu, D. Ma, Z. Shi, L. Zhu, D. Zhang, Y. Sun, M. Chrzanowski, S. Ma, Metal−organic framework based upon the synergy of a Brønsted acid framework and Lewis acid centers as a highly efficient heterogeneous catalyst for fixed-bed reactions, J. Am. Chem. Soc. 137 (2015) 4243−4248.
27. S.P. Desai, J. Ye, J. Zheng, M.S. Ferrandon, T.E. Webber, A.E. Platero-Prats, J. Duan, P. Garcia-Holley, D.M. Camaioni, K.W. Chapman, M. Delferro, O.K. Farha, J.L. Fulton, L. Gagliardi, J.A. Lercher, R.L. Penn, A. Stein, C.C. Lu, Well-defined rhodium–gallium catalytic sites in a metal–organic framework: Promoter-controlled selectivity in alkyne semihydrogenation to e-alkenes, J. Am. Chem. Soc. 140 (2018) 15309-15318.
28. Y. Liu, R.C. Klet, J. T. Hupp, O. Farha, Probing the correlations between the defects in metal-organic frameworks and their catalytic activity by an epoxide ring-opening reaction, Chem. Commun. 52 (2016) 7806-7809.
29. C.K. Brozek, M. Dinca, Ti^{3+}-, $V^{2+/3+}$-, $Cr^{2+/3+}$-, Mn^{2+}-, and Fe^{2+}-substituted MOF-5 and redox reactivity in Cr- and Fe-MOF-5, J. Am. Chem. Soc. 135 (2013) 12886-12891.

30. N. Portolés-Gil, S. Gómez-Coca, O. Vallcorba, G. Marbán, N. Aliaga-Alcalde, A. López-Periago, J.A. Ayllón, C. Domingo, Single molecule magnets of cobalt and zinc homo- and heterometallic coordination polymers prepared by a one-step synthetic procedure, RSC Adv. 10 (2020) 45090-45104.
31. A.S. Roy, J. Mondal, B. Banerjee, P. Mondal, A. Bhaumik, Sk. M. Islam, Pd-grafted porous metal–organic framework material as an efficient and reusable heterogeneous catalyst for C–C coupling reactions in water, Appl. Catal. A 469 (2014) 320-327.
32. B. Rungtaweevoranit, J. Baek, J.R. Araujo, B.S. Archanjo, K.M. Choi, O.M. Yaghi, G.A. Somorjai, Copper nanocrystals encapsulated in Zr-based metal−organic frameworks for highly selective CO_2 hydrogenation to methanol, Nano Lett. 16 (2016) 7645-7649.
33. F.R. Fortea-Perez, M. Mon, J. Ferrando-Soria, M. Boronat, A. Leyva-Perez, A. Corma, J.M. Herrera, D. Osadchii, J. Gascon, D. Armentano, E. Pardo, The MOF-driven synthesis of supported palladium clusters with catalytic activity for carbene-mediated chemistry, Nat. Mater. 16 (2017) 760-766.
34. M. Mon, M.A. Rivero-Crespo, J. Ferrando-Soria, A. Vidal-Moya, M. Boronat, A. Leyva-Pérez, A. Corma, J.C. Hernández-Garrido, M. López-Haro, J.J. Calvino, G. Ragazzon, A. Credi, D. Armentano, E. Pardo, Synthesis of densely packaged, ultrasmall Pt^0_2 clusters within a thioether-functionalized MOF: Catalytic activity in industrial reactions at low temperature, Angew. Chem., Int. Ed. 57 (2018) 6186−6191.
35. B. An, J. Zhang, K. Cheng, P. Ji, C. Wang, W. Lin, Confinement of ultrasmall Cu/ZnOx Nanoparticles in metal–organic frameworks for selective methanol synthesis from catalytic hydrogenation of CO_2, J. Am. Chem. Soc. 139 (2017) 3834-3840.
36. J. Fonseca, T. Gong, L. Jiao, H. Jiang, Metal–organic frameworks and their catalytic applications, from this: Metal–organic frameworks (MOFs) beyond crystallinity: amorphous MOFs, MOF liquids and MOF glasses, J. Mater. Chem. A 9 (2021) 10562.
37. M. Kubovics, S. Rojas, A.M. López-Periago, J. Fraile, P. Horcajada, C. Domingo, Fully supercritical CO_2 preparation of a nanostructured MOF composite with application in cutaneous drug delivery, J. Supercrit. Fluids 178 (2021) 105379.
38. A. Borras, G. Goncalves, G. Marban, S. Sandoval, S. Pinto, P.A.A.P. Marques, J. Fraile, G. Tobias, A.M. Lopez-Periago, C. Domingo, Preparation and characterization of graphene oxide aerogels: Exploring the limits of supercritical co_2 fabrication methods, Chem. Eur. J. 24 (2018) 15903-15911.
39. R.-P. Ye, J. Ding, W. Gong, M.D. Argyle, Q. Zhong, Y. Wang, C.K. Russel, Z. Xu, A.G. Russel, Q. Li, M. Fan, Y.-G. Yao, CO_2 hydrogenation to high-value products via heterogeneous catalysis, Nature Commun. 10 (2019) 5698.

40. M. Sanchez-Sanchez, I. deAsua, K. Diaz, Direct synthesis, structural features, and enhanced catalytic activity of the Basolite F300-like semiamorphous Fe-BTC framework, Cryst. Growth Des. 15 (2015) 4498-4506.
41. P. Horcajada, S. Surblé, C. Serre, D-Y. Hong, Y-K. Seo, J-S. Chang, J.M. Grenéche, I. Margiolakid, G. Férey, Synthesis and catalytic properties of MIL-100(Fe), an iron(III) carboxylate with large pores, Chem. Comm. (2007) 2820–2822.
42. A.M. López-Periago, C. Domingo, Features of supercritical CO_2 in the delicate world of the nanopores, J. Supercrit. Fluids 134 (2018) 204–213.
43. W. Hui Teoh, R. Mammucari, N.R. Foster, Solubility of organometallic complexes in supercritical carbon dioxide: A review, J. Organomet. Chem. 724 (2013) 102-116.
44. L-M. Cao, J. Zhang, X-F. Zhang, C-T. He, Confinement synthesis in porous molecule-based materials: a new opportunity for ultrafine nanostructures, Chem. Sci. 13 (2022) 1569-1593.
45. F. Salvador, C. Sánchez-Jiménez, M.J. Sánchez-Montero, A. Salvador, A review of the application of the BET equation to experimental data: the C parameter, Stu. Surf. Sci. Cat. 144 (2002) 379-386.
46. Q. Jiang, Y. Liu, T. Dintzer, J. Luo, K. Parkhomenko, A.-C. Roger, Tuning the highly dispersed metallic Cu species via manipulating Brønsted acid sites of mesoporous aluminosilicate support for CO_2 hydrogenation reactions, App. Cat. B: Env. 269 (2020) 118804.
47. Z. Chen, Q. Zhang, L. Huang, R. Li, W. Li, G. Xu, H. Cheng, Surface modification of ITO nanoparticles by trimesic acid: a combined experimental and DFT study, J. Phys. Chem. C, 118 (2014) 21244-21249.
48. X. Hu, J. Schuster, S.E. Schulz, T. Gessner, Surface chemistry of copper metal and copper oxide atomic layer deposition from copper(II) acetylacetonate: a combined first-principles and reactive molecular dynamics study, Phys. Chem. Chem. Phys. 17 (2015) 26892.
49. M. Palomba, G. Carotenuto, A. Longo, A brief review: The use of L-ascorbic acid as a green reducing agent of graphene oxide, Materials 15 (2022) 6456.
50. D. Yang, A. Velamakanni, G. Bozoklu, S. Park, M. Stoller, R.D. Piner, et al., Chemical analysis of graphene oxide films after heat and chemical treatments by X-ray photoelectron and Micro-Raman spectroscopy, Carbon 47 (2009) 145–152.
51. J.B. Benziger, R.J. Madix. Reactions and reaction intermediates on iron surfaces: II. Hydrocarbons and carboxylic acids, J. Catal. 65 (1980) 49–58.
52. B. Frank, R. Blume, A. Rinaldi, A. Trunschke, R. Schlögl, Oxygen insertion catalysis by sp^2 carbon, Angew. Chemie Int. Ed. 50 (2011) 10226–10230.
53. A. Borrás, J. Fraile, A. Rosado, G. Marbán, G. Tobias, A.M. López-Periago, C. Domingo, Green and solvent-free supercritical CO_2-assisted production of superparamagnetic graphene oxide

aerogels: Application as a superior contrast agent in MRI, ACS Sustainable Chem. Eng. 8 (2020) 4877−4888.

54. S. Nassreddine, G. Bergeret, B. Jouguet, C. Geantet, L. Piccolo, Operando study of iridium acetylacetonate decomposition on amorphous silica–alumina for bifunctional catalyst preparation, Phys. Chem. Chem. Phys. 12 (2010) 7812-7820.
55. H. Ando, Selective alkene production by the hydrogenation of carbon dioxide over Fe-Cu catalyst, Energy Proc. 89 (2016) 421-427.
56. Y. Mitsuka, N. Ogiwara, M. Mukoyoshi, H. Kitagawa, T. Yamamoto, T. Toriyama, S. Matsumura, M. Haneda, S. Kawaguchi, Y. Kubota, H. Kobayashi, Fabrication of integrated copper-based nanoparticles/amorphous metal–organic framework by a facile spray-drying method: Highly enhanced CO_2 hydrogenation activity for methanol synthesis, Angew. Chemie 133 (2021) 22457-22462.
57. A. Dhakshinamoorthy, M. Alvero, H. Garcia, Metal–organic frameworks as efficient heterogeneous catalysts for the regioselective ring opening of epoxides, Chem. A Eur. J. 16 (2010) 8530-8536.
58. A. Dhakshinamoorthy, M. Alvero, H. Garcia, Claisen–Schmidt condensation catalyzed by metal-organic frameworks, Adv. Syn. Cat. 352 (2010) 711-717.
59. F. Lu, X. Chen, W. Wang, Y. Zhang, Adjusting the CO_2 hydrogenation pathway via the synergic effects of iron carbides and iron oxides, Catal. Sci. Technol. 11 (2021) 7694–7703.
60. C. Karakaya, J. Parks II, Thermochemical processes for CO hydrogenation to fuels and chemicals: Challenges and opportunities, Applic. Energy Comb. Sci. 15 (2023) 100171.
61. S. Alireza-Valia, A. A. Markeba, J. Moral-Vicoa, X. Font, A. Sánchez, A novel Cu-based catalyst supported in chitosan nanoparticles for the hydrogenation of carbon dioxide to methanol: From the optimization of the catalyst performance to the reaction mechanism, Cata. Comm. 182 (2023) 106747.
62. H. Kobayashi, J.M. Taylor, Y. Mitsuka, N. Ogiwara, T. Yamamoto, T. Toriyama, S. Matsumura, H. Kitaqawa, Charge transfer dependence on CO_2 hydrogenation activity to methanol in Cu nanoparticles covered with metal-organic framework systems, Chem. Sci. 10 (2019) 3289-3294.